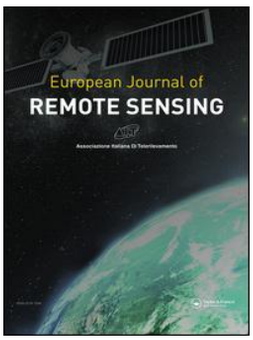

European Journal of Remote Sensing

ISSN: (Print) 2279-7254 (Online) Journal homepage: https://www.tandfonline.com/loi/tejr20

Aerial multispectral imagery for plant disease detection: radiometric calibration necessity assessment

Hossein Pourazar, Farhad Samadzadegan & Farzaneh Dadrass Javan

To cite this article: Hossein Pourazar, Farhad Samadzadegan & Farzaneh Dadrass Javan (2019) Aerial multispectral imagery for plant disease detection: radiometric calibration necessity assessment, European Journal of Remote Sensing, 52:sup3, 17-31, DOI: 10.1080/22797254.2019.1642143

To link to this article: https://doi.org/10.1080/22797254.2019.1642143

EUROPEAN JOURNAL OF REMOTE SENSING
2019, VOL. 52, NO. S3, 17–31
https://doi.org/10.1080/22797254.2019.1642143

Aerial multispectral imagery for plant disease detection: radiometric calibration necessity assessment

Hossein Pourazar, Farhad Samadzadegan and Farzaneh Dadrass Javan

School of Surveying and Geospatial Engineering, University College of Engineering, University of Tehran, Tehran, Iran

ABSTRACT

This paper focused on the necessity of radiometric calibration to distinguish diseased trees in orchards based on aerial multi-spectral images. For this purpose, two study sites were selected where multispectral images were collected using a multirotor UAV. The impact of radiometric correction on plant disease detection was assessed in two ways: 1) comparison of separability between the healthy and diseased classes using T-test and entropy distances; 2) radiometric calibration effect on the accuracy of classification. The experimental results showed the insignificant effect of radiometric calibration on separability criteria. In the second strategy, the experimental results showed that radiometric calibration had a negligible effect on the accuracy of classification. As a result, the overall accuracy and kappa values for un-calibrated and calibrated orthomosaic classifications of the citrus orchard were 96.49%, 0.941, 96.57% and 0.942, respectively, using five spectral bands as well as DVI, NDRE, NDVI and GNDVI vegetation indices using a random forest classifier. The experimental results were also similar at the other study site. Therefore, the overall accuracy and kappa values for the un-calibrated and calibrated orthomosaic classifications were 95.58%, 0.913, 95.56% and 0.913, respectively, using five spectral bands as well as NDRE, BNDVI, GNDVI, DVI, and NDVI vegetation indices.

ARTICLE HISTORY
Received 17 February 2019
Revised 13 June 2019
Accepted 8 July 2019

KEYWORDS
Multispectral; radiometric calibration; classification; plant disease; aerial imagery

Introduction

In recent years, the prediction of effective challenges on the crop yield such as climate change effects, diseases, and pests has become a critical issue in food managing strategies (Onisimo, Timothy, & Omer, 2017). Furthermore, because of the population increase and instability of agricultural production due to climate variability, some methods and techniques have been developed for monitoring the condition of plants as well as the quality and quantity of agricultural products.

Apparently, the inspection procedure for the early detection of the diseases is extremely time-consuming. Therefore, it is necessary to find a detection process which will be faster than the field inspection by experts (Psirofonia, Samaritakis, Eliopoulos, & Potamitis, 2017). The limitations of direct field inspection methods have led researchers to investigate remote sensing data to quickly and inexpensively obtain plant health information. Non-destructive remote sensing data permits measurement of biophysical and biochemical parameters of plants for non-destructive monitoring of plant growth and health (Lu et al., 2015; Sankaran, Ehsani, Inch, & Ploetz, 2012; Sankaran, Mishra, Ehsani, & Davis, 2010). These methods are based on the optical properties of plants and can be used for identifying nutrient deficiencies, plants diseases, water stress and excess water, insect damage, weeds, etc. (Baret, 2016; Haboudane, Miller, Pattey, Zarco-Tejada, & Strachan, 2004; Hede, Kashiwaya, Koike, & Sakurai, 2015; Sankaran et al., 2010). Combination of plant knowledge and remote sensing data can provide information for plant management and even initial advices about plant stress to prevent the spread of disease or pest infestation by adopting appropriate reactions in the early stages of stress.

In recent years, numerous remote sensing applications have been studied for monitoring the health of plants through using satellite (Jia et al., 2011; Li, Lee, Wang, Ehsani, & Yang, 2014), airborne (Hart & Myers, 1968; Huang, Lan, & Hoffmann, 2008; Katti, Lee, Ehsani, & Yang, 2015; Li et al., 2014; Ye, Sakai, ASADA, & Sasao, 2007) and ground-based (Ashourloo, Mobasheri, & Huete, 2014; Baranowski et al., 2015; Mishra, Karimi, Ehsani, & Albrigo, 2011; Ranjitha, Srinivasan, & Rajesh, 2014; Sankaran, Maja, Buchanon, & Ehsani, 2013; Sankaran, Mishra, Maja, & Ehsani, 2011) remote-sensed data. Multispectral images as well as related vegetation indices status ((Franke & Menz, 2007); (Jia et al., 2011); (Huang et al., 2008; Ye et al., 2007)) and hyperspectral images ((Glaser, Casas, Copenhaver, & Mueller, 2009); (Li et al., 2014), (Katti et al.,

CONTACT Farzaneh Dadrass Javan fdadrasjavan@ut.ac.ir School of Surveying and Geospatial Engineering, University College of Engineering, University of Tehran, Tehran, Iran

2015)) are used in the airborne and space-borne remote sensing to study the health of plants. Ground-based remote sensing data is usually used to identify the best wavelengths along with optimum vegetation indices related to the effect of pest, disease and nutrient deficiency in plants with high correlation ((Sankaran et al., 2011) (Ashourloo et al., 2014). (Ranjitha et al., 2014) (Baranowski et al., 2015)). More recently, in the remote sensing application, manned airborne vehicles are replaced with unmanned aerial vehicles (UAVs), which can be deployed quickly and repeatedly, and also have flexible flying height and timing of missions as well as high-resolution imagery (Wójtowicz, Wójtowicz, & Piekarczyk, 2016).

One of the main steps of image post-processing in remote sensing applications is the extraction of absolute reflectance measurements from the data in the radiometric calibration process (Kelcey & Lucieer, 2012). It should be noted that the necessity of camera calibration is an open question. Therefore, this study investigated the potential of UAV-based multispectral imagery in plant disease detection and especially concentrated on the necessity of radiometric calibration.

The first study area was a citrus orchard with the Greening disease. The citrus Greening disease has become one of the greatest challenges for citrus growers across the world (Cevallos-Cevallos, Futch, Shilts, Folimonova, & Reyes-De-Corcuera, 2012). Citrus Greening, transmitted by grafting from citrus to citrus, can severely weaken citrus trees, causing reductions in fruit yield and quality. A sample of Greening symptoms on citrus tree leaves is presented in Figure 1(a).

The other study area is a peach orchard with the peach leaf curl (PLC) disease. The PLC fungal disease is one of the most common diseases of peach trees in the north of Iran that mostly affects peaches leaves and nectarines. PLC is caused by the ascomycetous fungus Taphrina deformans and causes parts of individual peach leaves to become curled and pale green or reddish in color (Figure 1(b)) (Moscatello et al., 2017). Taphrina deformans primarily affects a foliage, but may also affect fruits and young twigs (Pecknold, 2015).

Related works

The fast technology development in UAV systems and the advent of small-scale UAVs, which can carry small visible and multispectral sensors, provide the opportunity to capture high spatial and spectral resolution data, especially for agricultural application. In multispectral images, a variety of spectral bands offer the extraction of vegetation indices to distinguish diseased and healthy plants (Agüera, Carvajal, & Pérez, 2011; Albetis et al., 2017; Candiago, Remondino, De Giglio, Dubbini, & Gattelli, 2015; De Castro, Ehsani, Ploetz, Crane, & Abdulridha, 2015; Garcia-Ruiz et al., 2013; Sarkar, Das, Ehsani, & Kumar, 2016; Wójtowicz et al., 2016).

To investigate the potential of the nutrient deficiency using UAV-based multispectral images, Agüera et al. compared the correlation between the calculated NDVI from UAV-based multispectral images and the ground-based multispectral radiometer with the nitrogen status in a sunflower field (Agüera et al., 2011). Results proved a higher correlation coefficient (R = 0.80) using the UAV platform than a ground-based measurement (R = 0.71). In another study, Garcia-Ruiz et al. investigated the capability of UAV-based multispectral images using for citrus greening detection in comparison with similar images captured based on piloted aircraft (Garcia-Ruiz et al., 2013). They achieved a classification accuracy of 67–85% and 61–74% based on UAV-based and aircraft-based datasets, respectively, using six spectral bands as well as NDVI, GNDVI, SAVI, NIR–R, R/NIR, green(G)/R and NIR/R vegetation indices. To detect the citrus Greening disease, Sarkar et al. also presented an UAS sensor set including an onboard active spectrally selective light source and an RGB-D sensor that measures distance and reflectance of rotated polarized

Figure 1. (a) Greening symptoms on citrus tree leaves; (b) the PLC sample.

light (Sarkar et al., 2016). They used a liner SVM classifier and reported 93% classification accuracy.

De Castro et al., evaluated the spatial and spectral of multispectral requirements of images for quick and accurate detection of laurel wilt (LW) disease in an avocado field, considering the change in the flight altitudes and spectral sensors. Results demonstrated that most effective spectral wavelengths were 580–10 nm, 650–10 nm, 740–10 nm, 750–10 nm, 760–10 nm and 850–40 nm with 15.3 cm spatial resolution and the optimum vegetation indices were TCARI760–650, GNDVI, NIR/G, Redge/G and VIGreen using Redge or NIR bands (De Castro et al., 2015).

Albetis et al. evaluated the capability of spectral features computed from the UAV multispectral imagery including spectral bands, vegetation indices and biophysical parameters for discriminating the Flavescence doréesymptoms disease in red and white cultivars from healthy vine vegetation. Results presented best with red cultivars, but were not acceptable for white cultivars (Albetis et al., 2017).

The radiometric calibration of the UAV-based multispectral images is one of the main steps of image processing in remote sensing applications (Kelcey & Lucieer, 2012). For the purpose, especially in UAV-based remote sensing applications, usually an image-based empirical approach, called empirical lines based methods, is used (Berni, Zarco-Tejada, Suárez, & Fereres, 2009). This technique is based on the assumption of an empirical relationship between the image DNs and the at-surface reflectance which is made as a field measure of the appropriate targets (Smith & Milton, 1999).

Kelcey and Lucieer for radiometric calibration of UAV-based multispectral images of mini-MCA camera, used three radiometric targets made of a plywood and backing with a white paperish fabric (Tyvek), grey fabric and black fabric covers. The targets' at-surface reflectance were measured by an ASD HandHeld 2 Portable Spectrometer (Kelcey & Lucieer, 2012). In the study, two black and white calibration targets with 3% and 82% reflectance, respectively, were used during flight for radiometric correction in empirical line calibration method which was carried out in ENVI software (De Castro et al., 2015).

On the other hand, along with a UAV-based multispectral cameras, a white calibration panel is usually provided for radiometric calibration. Miura and Huete evaluated three white calibration panel-based radiometric calibration methods in the hypersonic airborne data, called "reflectance mode", "linear interpolation" and "continuous panel" (Miura & Huete, 2009). These methods used white calibration panel to convert DN to at-surface reflectance. Clemens modified the "reflectance mode" method from Miura and Huete (2009) to reduce the reflectance value conversion bias (Clemens, 2012). In this study, an average of the pre- and post-flight panel readings in the reflectance conversion is used which assumed a linearity due to the short time of flight. Garcia-Ruiz et al. used whiteboard for radiometric calibration of the UAV-based images to ensure that 100% reflectance corresponding with a digital number of 255 (Garcia-Ruiz et al., 2013). Albetis et al. also used the calibrated ground panel, before and after the flight, to convert the DN to at-surface reflectance in each band (Albetis et al., 2017).

As shown in the literature, radiometric calibration is considered as the main step in UAV-based plant disease detection, and measurements of reference targets are implemented in empirical line-based methods by default, while the efficacy and necessity of this step is unclear. Therefore, the efficacy and necessity of the radiometric calibration step in plant disease detection using UAV-based multispectral images were investigated in this study.

Materials and methods

Study area and imaging system

Two different agricultural fields located in the north and south of Iran were selected as the study area. The first one, a citrus orchard outbreak with Greening disease, is located in Fasa County, Fars Province, Iran (Figure 2(a)). The second field is located in Neka City, Mazandaran Province, Iran, which is a peach orchard affected by the PLC disease (Figure 2(b)).

A small multirotor platform that is equipped with Micasense RedEdge multispectral camera, which is especially designed for agriculture applications, is selected for imaging of both test fields. A summary on the specifications of both platform and imaging system is presented in Table 1.

To achieve reliable and efficient multispectral images, accurate flight planning is needed in order to achieve optimum image resolution and accuracy at the best flight time and cost. Some details on the flight planning parameters in the both study areas are presented in Table 2.

Disease and healthy trees as ground truth were selected by the experts' visual inspection and labeled using special targets (Figure 5) before image acquisition to train and test the classifier. Therefore, 15 citrus Greening infected and 10 healthy trees at the Fasa study area as well as 20 PLC infected and 12 healthy trees at the other study area were selected as ground truth data.

Processing methodology

Figure 3 summarizes the workflow of proposed methodology for plants disease detection based on

Figure 2. a) First data set; Citrus orchard in Fasa, b) Second data set; Peach orchard in Neka.

Table 1. Platform and imaging system specifications.

Platform		Multispectral sensor	
Platform Type	Hexa-copter	Spectral bands	Blue- Green-Red-RE-NIR
Flight Duration	40 min	size	12.1 x 6.6 × 4.6 cm
Dimension	1.2 m	weight	150g
Max takeoff weight	6 kg	Field of view	47.2 ° HFOV
Max Flight Altitude	200m AGL	Focal length	5.5 mm
		radiometric resolution	12-bit RAW

Table 2. The flight planning parameters of the study sites.

	Fasa	Neka
Flight Altitude (m)	25	10
Area (m^2)	16.2e+03	3.44e+03
Flight Time (min)	~17	~15
Ground Resolution (mm/pix)	12.7	6.43
Number of Images	494	760
No of Strips	20	17
Footprint (m2)	16.25x12.45	8.23x6.17
Overlap	75%	80%
Sidelap	75%	70%

multispectral imagery and assessment of radiometric calibration evaluation necessity.

Acquired multilens images were registered band-to-band in the first step and then aligned in the bundle adjustment process. Regarding the image acquisition under different illumination conditions, the normalization of image blocks is necessary in order to produce homogeneous block which is done based on radiometric block adjustment. Finally, Band registered aligned Images stitched together to produce orthomosaic. In (Albetis et al., 2017; De Castro et al., 2015; Garcia-Ruiz et al., 2013; Honkavaara et al., 2013; Kelcey & Lucieer, 2012; Wijesingha, 2016), commonly radiometric calibration is done as the main step that converts DN to reflectance. In order to evaluate the radiometric calibration necessity of multispectral images and to inspect its effects on the quality of final results, classification process is performed both on DN (Strategy II) and reflections based data (Strategy I) and results were evaluated and discussed. The classification process consisted of three main steps: feature space generation; train classifier and performs classification to generate disease map.

Band-to-band registration

Recent developed UAV-based multispectral cameras are usually composed of multilens structure (Figure 4). Due to the low altitude of flight in small UAV, Band miss-registration of multispectral images acquired by multi-lenses cameras is a great challenge (Jhan, Rau, & Huang, 2016). In this study, SIFT[1] algorithm is applied to extract corresponding features from images. It is well suited for the feature detection and description because it is able to handle the special characteristics of the input data such as low image contrast as well as rotation, translation and scale differences (Lindeberg, 2012).

[1]Scale Invariant Feature Transform.

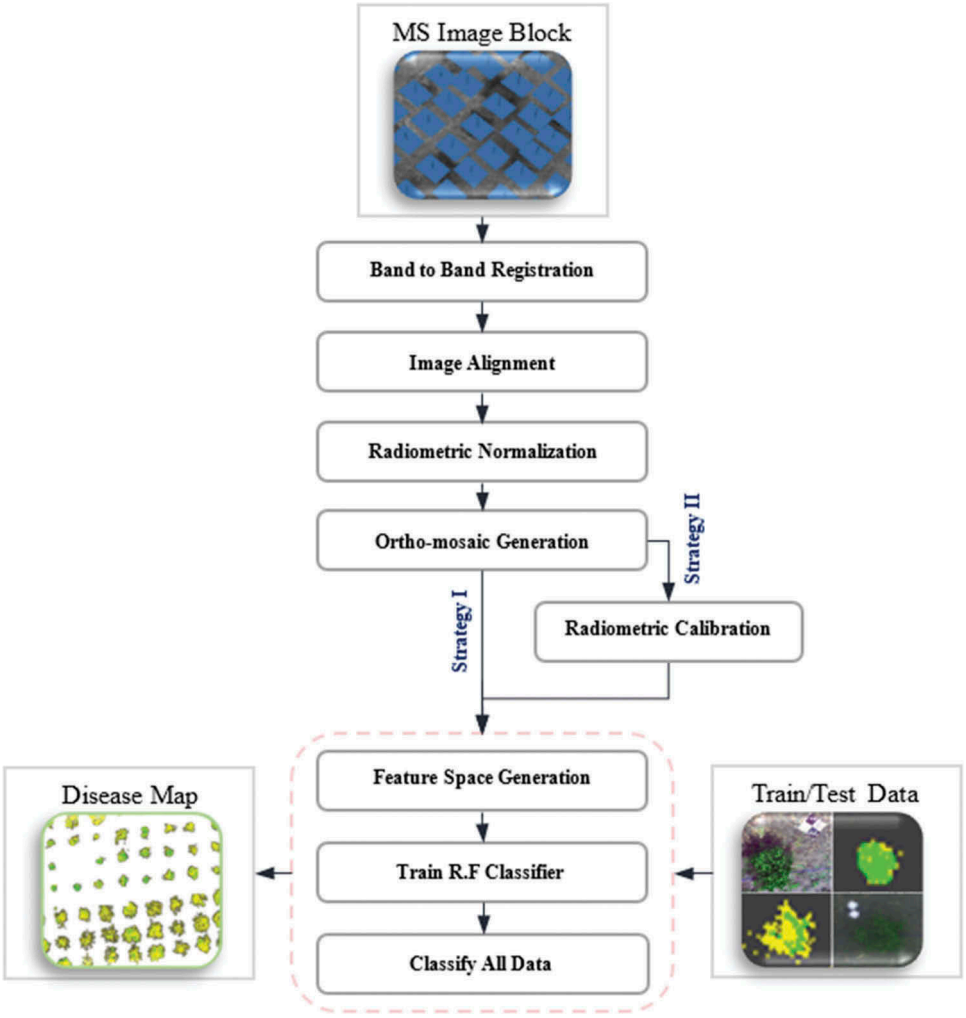

Figure 3. Data processing flow diagram. strategy I: Processing without radiometric calibration; strategy-II: Processing based on reflectance orthomosaic by perform radiometric calibrated.

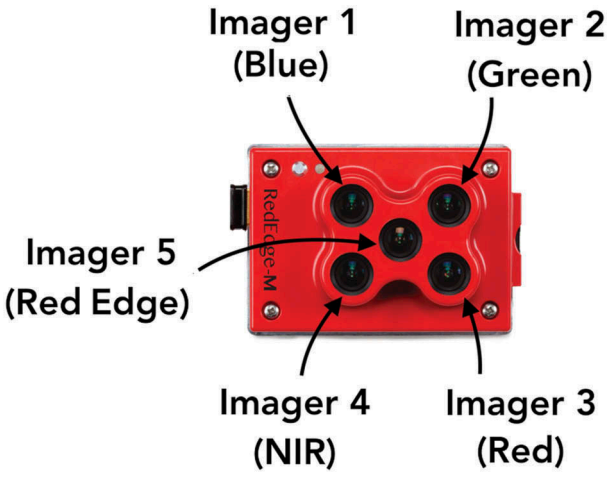

Figure 4. The MicaSense RedEdge as an advanced multilens and multispectral camera specially designed for small UAVs.

After the extraction of feature points using SIFT algorithm, the matching process can be done by comparing the minimum Euclidean distance between the extracted feature vectors. With the matched features, the mathematical relationship between the two images will be computable. Finally, the images were registered and resampled based on the projection transformation (Shi, Wang, & Xu, 2011).

Image alignment

Image alignment provides interior and exterior orientation parameters in the bundle adjustment process that use tie points in overlapping images (Nissen, Johnson, Fitzgerald, Morgan, & White, 2014). Tie points could be extracted by the SIFT algorithm. The SIFT algorithm detects features and matches corresponding features in overlapping images; moreover, outliers and improper matches are eliminated simultaneously (Nesbit, 2014). Thus, a sparse point cloud will be an output of the bundle adjustment (Wijesingha, 2016). This process is carried out effectively due to consideration of sufficient overlap and side laps of images during a flight mission.

Radiometric normalization

Regarding the image acquisition under different illumination conditions, the radiometric normalization of image blocks is necessary in order to produce homogeneous orthomosaic. According to Gehrke

and Beshah (2016), the radiometric normalization parameters for all images in the block are computed in the least-squares adjustment using radiometric tie points. The main observation equation for each radiometric tie point (extracted geometric tie points in image alignment step) between two images can be expressed as Equation (1):

$$0 = \{c_{xy}DN_{xy} + b_{xy}\}_{ImgA} - \{c_{xy}DN_{xy} + b_{xy}\}_{ImgB} \quad (1)$$

where c_{xy} and b_{xy} are the normalization parameters. For the radiometric control points on the reference image, Equation (1) is rewritten as Equation (2):

$$\{DN_{xy}\}_{RefImg} = \{c_{xy}DN_{xy} + b_{xy}\}_{AdjImgA} \quad (2)$$

Radiometric control points were applied to define the "radiometric datum" (Gehrke & Beshah, 2016).

Orthomosaic generation

Because of the small footprint of each image, the acquired images were geometrically corrected and merged to produce a seamless orthomosaic of the whole area.

In UAV imagery-based applications, dense point cloud extraction based on the aligned images is a main step commonly (Candiago et al., 2015; Näsi et al., 2015; Nevalainen et al., 2017; Wijesingha, 2016). Finally, orthomosaic was generated based on aligned images and dense point cloud; Thus, the topographic relief of trees was considered there. However, in this study, an orthomosaic without trees topographic relief consideration satisfied our goals. Therefore, orthomosaic is generated based on aligned images and one coarse DSM producing from the sparse point cloud.

Radiometric calibration

One of the main steps in image processing for remote sensing applications is the radiometric calibration process where the absolute reflectance measurements from the DN data is extracted (Kelcey & Lucieer, 2012). Acquired images could be calibrated using radiometric reference images that captured from a calibrated reflectance panel before and after each flight (Clemens, 2012).

In this study, "reflectance mode" method is applied for radiometric calibration based on Clemens (2012). In the Clemens method, an average of the pre- and post-flight panel measurements is used in the reflectance conversion. Equation (3) presents the basis of the reflectance factor calculation in the reflectance mode method.

$$R_T = \frac{DN_T}{DN_R} R_R \quad (3)$$

where DN_T is digital numbers of the target; DN_R is the average of the pre- and post-flight in reference in images; and R_R is the reflectance factor of the white panel which will determine R_T, the reflectance factor of the unknown surface.

Feature space generation

One of the simplest techniques to map the vegetation is to use vegetation indices that are easily calculable and understandable (P. C. Joshi, 2011). Numerous vegetation indices are calculated as the difference or ratio of two or several bands in the wide range of the spectrum (e.g. NDVI, RVI, etc.). They constitute the simple and straight method to extract highly correlated information to biophysical parameters of plants from remotely sensed data. After extraction of ortho images, spectral features including five spectral bands and 12 vegetation indices were extracted to be applied in the classification (Table 3). In Table 3, B, G, R, RE, and NIR are the blue, green, red, red edge, and near infrared bands of the multispectral images, respectively.

After calculating the spectral features, the most suitable features that discriminated between the healthy and unhealthy trees were selected in this study. Decreasing the number of features, increases the generalization capability and reduces the computational complexity of the classification algorithm (Guyon & Elisseeff, 2003). The T-test and entropy distances measure the separability between two classes and can be used as criteria to evaluate the efficacy of each feature for discriminating between healthy and unhealthy trees classes.

Classification

After feature space generation, the final step towards health map generation is the classification of images based on selected training data. For this purpose, a random forest classifier, developed by Breiman (2001), is used due to its simplicity and high performance (Feng, Liu, & Gong, 2015; A. Joshi, Monnier, Betke, & Sclaroff, 2015). Random forests non-parametric

Table 3. Applied vegetation indices.

Index	Formula	Reference
Ratio Vegetation Index	$RVI = \frac{NIR}{R}$	[50]
Normalized Difference Vegetation Index	$NDVI = \frac{NIR-R}{NIR+R}$	[17, 51]
Green Normalized Difference Vegetation Index	$GNDVI = \frac{NIR-G}{NIR+G}$	[52]
Green Ratio Vegetation Index	$GRVI = \frac{NIR}{G}$	[53]
Blue Normalized Difference Vegetation Index	$BNDVI = \frac{NIR-B}{NIR+B}$	[54]
Red Edge Normalized Difference Vegetation Index	$NDRE = \frac{NIR-RE}{NIR+RE}$	[17, 55]
Infrared Percentage Vegetation Index	$IPVI = \frac{NIR}{NIR+R}$	[56]
Structure Insensitive Pigment Index	$SIPI = \frac{NIR-B}{NIR-R}$	[17, 57]
Optimized Soil-Adjusted Vegetation Index	OSAVI = (NIR-R)/(NIR +R + 0.16)	[9]
Chlorophyll Index	$CI = \frac{NIR}{G} - 1$	[58, 59]
Difference Vegetation Index	DVI = NIR-R	[60]
Greenness Index	$GI = \frac{G}{R}$	[61]

classifier is an ensemble-based machine-learning algorithm that engages the multiple decision tree classifiers in a voting strategy to provide the final prediction. It consists of several decision tree classifiers that build using a bootstrap sample of the data with a random variable set at each node to split on.

Implementation of random forest classifiers requires a few parameters, including the number of trees and the number of randomly selected predictor variables (Rodriguez-Galiano, Ghimire, Rogan, Chica-Olmo, & Rigol-Sanchez, 2012). So random forest offer less complex computations and running time, as well as high performances in the computer vision domain especially (REZAEIAN, AMIRFATTAHI, & SADRI, 2014). In this study, we used a random forest classifier consisting of 100 decision trees.

The final accuracy in detection of the diseased and healthy trees is tested by calculating error matrices of the test data (references). The error matrix presents the error of omission, error of commission, overall accuracy and kappa (κ) values (references).

Experiments and results

In this study, we evaluated the impact of radiometric calibration on UAV-based multispectral plant disease detection using the two datasets with different diseases and environmental conditions. For this, 557 images from the Fasa test area and 683 images from the Neka test area were captured based on the flight plan.

Band-to-band registration

The first processing step is spectral bands registration of images. Due to the multilenses structure of a multispectral camera, a considerable geometric displacement between images captured by lenses appeared. To remove the displacements, the R band was selected as the master and the rest were considered as slaves which should be registered to the master. The band registration of all the images were conducted based on the proposed strategy and the RMSE value of 0.4 pixels was available based on the target measurement. Figure 5 shows two false color images of the same scene: original image and band registered image as a sample.

Image alignment and seamless orthomosaic generation

After band registration step, a seamless orthomosaic of the whole area covering in the imagery step should be generated with five spectral bands. For this purpose, multispectral images must be aligned. In this step, geometric tie points were extracted, and image interior and exterior parameters were estimated. Table 4 presents the summary of the block adjustment parameters.

Based on the aligned band registered images, a dense point cloud was produced and used in orthomosaics generation. The specification of the dense point cloud and orthomosaics are presented in Table 5. The generated orthomosaics are depicted in Figure 6.

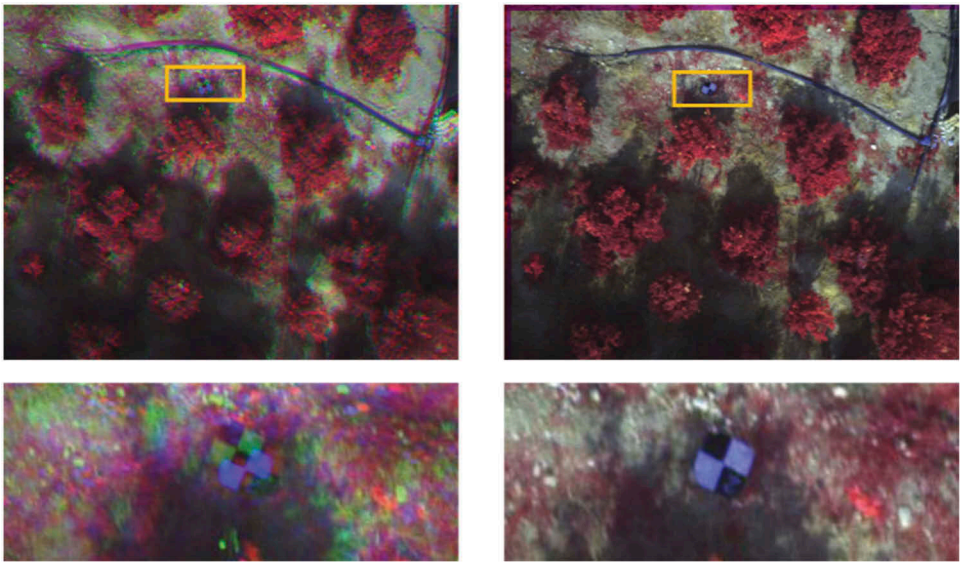

Figure 5. Spectral bands registration of Micasense RedEdge camera images; Left: uncorrected, Right: Corrected.

Table 4. Summary of the block adjustment parameters.

	Fasa Site	Neka Site
Number of images	1470	3800
Tie points	2,529,731	2,534,329
RMS reprojection error	(0.66246 pix)	(0.85034 pix)
Max reprojection error	(31.9115 pix)	(27.3773 pix)

Table 5. Specification of dense point clouds and orthomosaics.

		Fasa Site	Neka Site
Orthomosaic	Resolution(cm/pix)	1.27	0.643
	Size (pixel)	12713x15413	7485x15283
Dense Point Cloud	Size (point)	26,909,315	25,386,097

As is depicted in Figure 6, a seamless orthomosaics was generated after radiometric normalization which was prepared for the feature extraction and classification processing step.

Radiometric calibration

For the radiometric calibration process, reference images of a white panel were captured immediately before and after each flight. A sample image acquired from the calibrated reflectance panel is presented in Figure 7.

Maximum DNs in the images captured from the white panel, before and after the flight (BF and AF, respectively), are listed in Table 6 for the both study data sets. Note that the sensor outputs 12-bit data are stored as 16-bit TIFFs.

DNs values are related with at-sensor radiance directly; Thus, Table 6 shows the decrease in at-

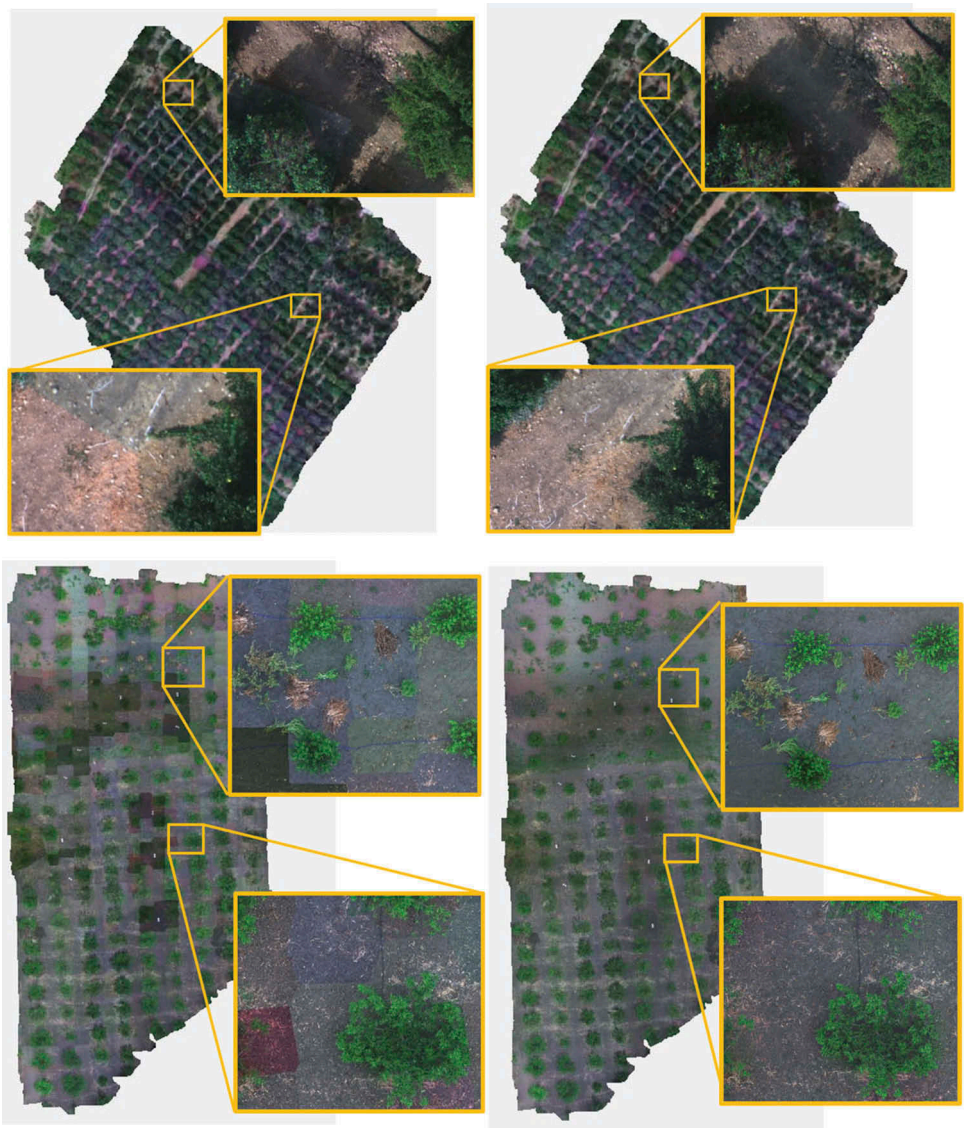

Figure 6. Left up: Fasa study site orthomosaic without radiometric normalization, Right Up: Fasa study site orthomosaic with radiometric normalization. Left down: Neka study site orthomosaic without radiometric normalization, Right down: Neka study site orthomosaic with radiometric normalization.

Figure 7. Left: reflectance panel image acquisition, right: Red edge band captured from reflectance panel.

Table 6. The maximum DN of the white panel in the five spectral bands.

	Fasa Site		Neka Site	
Spectral Band	BF	AF	BF	AF
Blue	57,488	55,424	52,000	32,320
Green	59,152	58,304	47,744	34,480
Red	54,480	53,248	42,816	28,128
NIR	58,048	55,280	44,208	29,696
RedEdge	59,472	53,696	44,624	26,784

sensor radiance during the both flights. The rate of this reduction was much higher at the Neka site, which indicated a significant change in illumination conditions during that flight. The mean DN values of BF and AF were used in Equation (3) to calculate the reflectance-based values and new orthomosaics were generated based on these new values for each study data.

Spectral feature analysis

Feature space in our study includes five spectral bands (B, G, R, RE, and NIR) and 12 vegetation indices (RVI, NDVI, GNDVI, GRVI, BNDVI, NDRE, IPVI, SIPI, OSAVI, CI, DVI and GI).

In order to investigate the necessity of sensor calibration for vegetation disease detection, separability between healthy and un-healthy tree classes, related features were investigated using T-test and entropy criteria using ground truth data collected from the calibrated and un-calibrated data for the both study areas. The experimental results are presented in Figure 8.

Considering the achieved values presented in Figure 8, it can be concluded that the camera calibration did not have any effects on the result based on T-test and entropy distances. However, comparing the extracted feature values in ground truth data

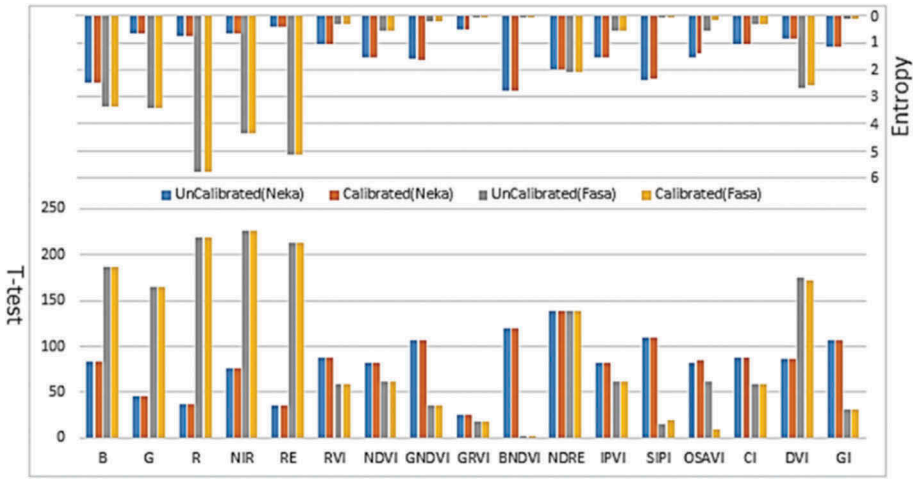

Figure 8. The distance between healthy and un-healthy classes based on T-test and entropy criteria in ground truth data collected from calibrated and un-calibrated based orthomosaics.

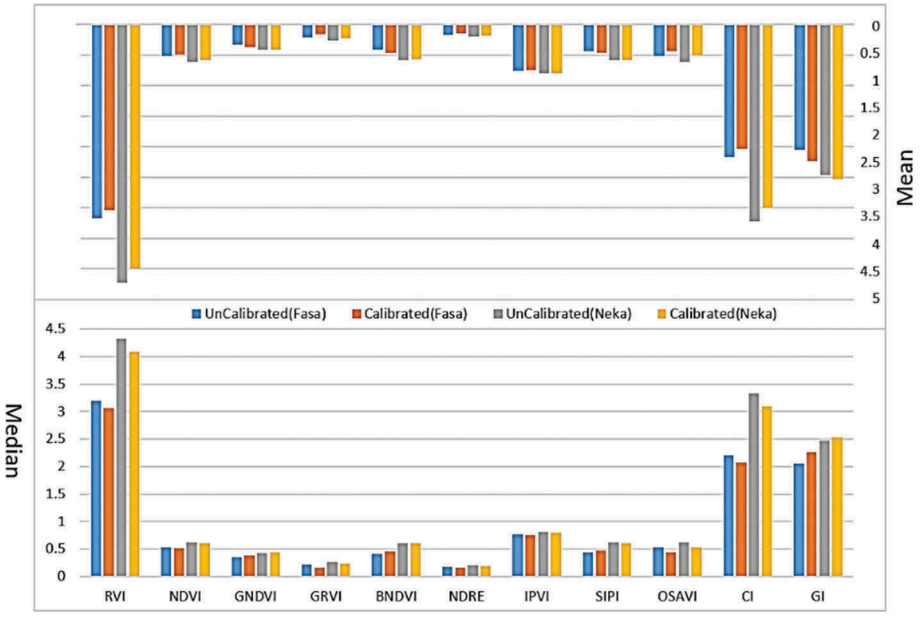

Figure 9. The feature values in ground truth data collected from calibrated and un-calibrated based orthomosaics.

measured in calibrated and un-calibrated orthomosaics states partly different values in the both study areas (Figure 9).

Classification

Three main classes were determined as un-healthy trees, healthy trees and non-trees at the study sites. Using the red and near infra-red spectral bands, the non-tree class was easily separated exactly from the trees classes. However, the detection of healthy and un-healthy trees classes remained as the main challenge.

Five spectral bands, as well as some VI that have high discrimination between healthy and un-healthy classes based on T-test and entropy criteria (Figure 8) and low correlation together (Table 7) were used in a random forest classifier consisting of 100 decision trees.

From Table 7, it is obvious that there were higher correlations between RVI, NDVI, IPVI, OSAVI, and CI, between BNDVI and SIPI, and between GNDVI and GI; similar results were obtained for the other study site.

At the Fasa study site, five spectral bands as well as DVI, NDRE, NDVI, and GNDVI vegetation indices were used in the classification process of un-calibrated and calibrated orthomosaics. Figure 10 shows the generated map of the healthy and Greening infected trees and non-trees. There was an insignificant difference in the classification maps (Figure 10). Small differences in results were observable, although were not significant.

The overall accuracy and kappa values for un-calibrated and calibrated based orthomosaic classifications were 96.49%, 0.941, 96.57% and 0.942, respectively. The confusion matrix and estimated user's and producer's accuracy measures are also presented in Table 8 (un-calibrated orthomosaic) and Table 9 (calibrated orthomosaic).

At the Neka study site, classification of the un-calibrated and calibrated orthomosaics is performed using five spectral bands as well as NDRE,

Table 7. Vegetation indices correlations at the Fasa study site.

	RVI	NDVI	GNDVI	GRVI	BNDVI	NDRE	IPVI	SIPI	OSAVI	CI	DVI	GI
RVI	1.0000	0.9747	0.6263	0.2655	0.5205	0.5056	0.9747	0.7575	0.9450	1.0000	0.3300	0.6213
NDVI		1.0000	0.6410	0.2651	0.5340	0.5147	1.0000	0.7743	0.9653	0.9747	0.3277	0.6133
GNDVI			1.0000	−0.5672	0.6327	0.7706	0.6410	0.7139	0.5748	0.6263	0.0137	0.9757
GRVI				1.0000	−0.2257	−0.4167	0.2651	−0.0685	0.3106	0.2655	0.3321	−0.576
BNDVI					1.0000	0.4172	0.5340	0.9468	0.5358	0.5205	0.2240	0.6276
NDRE						1.0000	0.5147	0.5069	0.3437	0.5056	−0.421	0.7549
IPVI							1.0000	0.7743	0.9653	0.9747	0.3277	0.6133
SIPI								1.0000	0.7622	0.7575	0.2892	0.6999
OSAVI									1.0000	0.9450	0.5552	0.5536
CI										1.0000	0.3300	0.6213
DVI											1.0000	0.0227
GI												1.0000

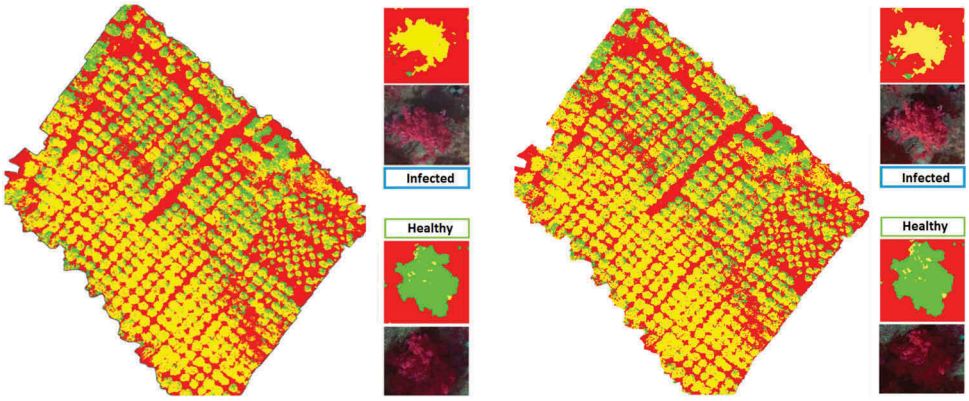

Figure 10. The classification map of healthy trees (green), Greening infected trees (yellow) and non-trees (red) based on the un-calibrated (Left) and calibrated (Right) orthomosaics at the Fasa study site.

Table 8. The confusion matrix and estimated user's and producer's accuracy of un-calibrated orthomosaic at the Fasa site.

Confusion Matrix				
		Classified Data		
		Disease	Healthy	Non-tree
Test Data	Disease	97.30%	2.55%	0.14%
	Healthy	17.16%	82.84%	0.00%
	Non-tree	0.03%	0.00%	99.97%

User's and Producer's Accuracy		
Class/Accuracy	User (%)	Producer (%)
Un-healthy	92.31	97.30
Healthy	93.84	82.84
Non-tree	99.91	99.97

Table 9. The confusion matrix and estimated user's and producer's accuracy of calibrated orthomosaics at the Fasa site.

Confusion Matrix				
		Classified Data		
		Disease	Healthy	Non-tree
Test Data	Disease	96.87%	03.02%	00.11%
	Healthy	15.88%	84.12%	00.00%
	Non-tree	00.03%	00.00%	99.97%

User's and Producer's Accuracy		
Class/Accuracy	User (%)	Producer (%)
Un-healthy	92.89	96.87
Healthy	92.83	84.12
Non-tree	99.93	99.97

BNDVI, GNDVI, DVI, and NDVI vegetation indices. Figure 11 the classification result of healthy, Leaf Peach Curve infected and non-trees at the Neka study site. As in the Fasa data set, no significant difference in the classification map is observable (Figure 11).

Achieved overall accuracy and kappa values for the un-calibrated and calibrated orthomosaic classifications were 95.58%, 0.913, 95.56% and 0.913, respectively. The confusion matrix and estimated user's and producer's accuracy measures are also computed and presented in Tables 10 and 11, respectively.

Inspecting results, it can be concluded that radiometric calibration of images has a minor effect on the classification accuracy. In the both statuses, almost the same precision was achieved and the confusion matrix components were not significantly different.

Discussion

Radiometric calibration is mentioned as one of the main steps in UAV-based plant disease detection, and measurements of reference targets are implemented in empirical line-based methods by default. To study the necessity of this process, in this paper, two study data with different environmental conditions and affected by different diseases were classified to generate a tree health state map. Therefore, different processing steps were analyzed and the focus was on the necessity of radiometric calibration.

The multi-lenses structure of the multispectral camera in low flight altitude missions created a considerable geometric displacement between the spectral bands (Figure 5) which is up to 25 pixels for our data. Here, the maximum height difference is about 10 m. Ignoring this displacement will result in different spectral features for the same objects and will lead to unsuitable training data. Therefore, the band-to-band registration step is important in the application; here, even leaf size is important and will reduce the registration error up to an average RMSE of 0.4 Pixel. It has to be mentioned that in images with extremely small relief variances with respect to flight height or with not much small focusing elements, the registration process can be neglected. In this situation, the ortho generation process can reduce the displacement to an acceptable level.

Orthomosaic is generated based on aligned images with the accuracy of 0.85 pixel and generated a dense point cloud. However, different illumination conditions in each capturing station heterogeneous final

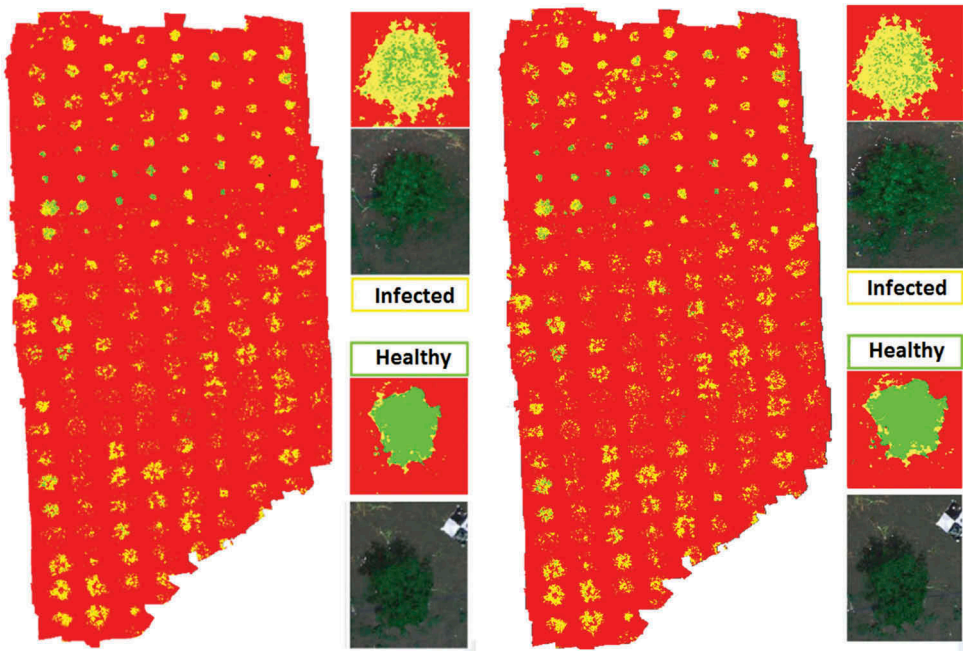

Figure 11. The classification map of healthy trees (green), leaf peach curve infected trees (yellow) and non-trees (red) or the un-calibrated (left) and calibrated (right) orthomosaics at the Neka study site.

Table 10. The confusion matrix and estimated user's and producer's accuracy of un-calibrated orthomosaic at the Neka site.

Confusion Matrix				
		Classified Data		
		Disease	Healthy	Non-tree
Test Data	Disease	84.14%	15.19%	00.67%
	Healthy	09.68%	89.01%	00.23%
	Non-tree	00.16%	00.01%	99.86%

User's and Producer's Accuracy		
Class/Accuracy	User (%)	Producer (%)
Disease	85.84	84.14
Healthy	88.94	90.08
Non-tree	99.78	99.83

Table 11. The confusion matrix and estimated user's and producer's accuracy of calibrated orthomosaics at the Neka site.

Confusion Matrix				
		Classified Data		
		Disease	Healthy	Non-tree
Test Data	Disease	84.41%	14.79%	00.80%
	Healthy	09.99%	89.77%	00.23%
	Non-tree	00.14%	00.01%	99.85%

User's and Producer's Accuracy		
Class/Accuracy	User (%)	Producer (%)
Disease	85.45	84.41
Healthy	89.26	89.77
Non-tree	99.75	99.85

orthomosaics (Figure 6-Left) and corrupts training data like the previous step.

The next step to prepare the training data is radiometric calibration which is performed based on empirical lines and changes pixel values linearly in each band. Therefore, outputs of this step can change the spectral features values. As shown in Figure 9, variation in most of the VIs is small due to their relative nature.

The detection of the healthy and unhealthy tree classes was performed using a random forest classifier. For this purpose, feature space was produced, including five spectral bands and 12 vegetation indices. The best features were selected based on the separation criteria of the tree classes and the correlation between the features. The correlation ranges from 94.5% to 100% between RVI, NDVI, IPVI, OSAVI, and CI, is 94.7% between BNDVI and SIPI, and is 97.6% between GNDVI and GI (Table 7); thus, six features can be eliminated. Moreover, at the Fasa study site, the spectral bands DVI and NDRE made the highest separation whereas the spectral band BNDVI made the lowest separation between the healthy and unhealthy tree classes. On the other hand, at the Neka study site, NDRE and BNDVI made the highest separation while GRVI made the lowest separation between classes. Classification was carried out using the selected features, and results are presented in Table 8 to Table 11. At the Fasa study site, citrus orchard with the greening disease, the overall accuracy and kappa values for the un-calibrated and calibrated orthomosaic classifications were 96.49%, 0.941, 96.57% and 0.942, respectively. Similarly, the experimental results at the Neka study site with PLC yielded the same conclusions. The overall accuracy and kappa values for the un-calibrated and calibrated orthomosaic classifications were 95.58%, 0.913, 95.56% and 0.913, respectively.

However, because of the linear structure of radiometric calibration, separation of the healthy and unhealthy tree classes based on t-test and entropy criteria did not change using the most spectral features (Figure 8); consequently, there were insignificant differences in the classification results after radiometric calibration.

Conclusions

This study investigated the necessity of radiometric calibration in UAV-based multispectral imagery for plant tree disease detection and classification applications. For this purpose, two study sites with different conditions of climate, date, tree species and disease types were selected and multispectral images were captured using a RedEdge camera mounted on a multirotor UAV.

Due to the multi-lens structure of the camera and the low flying altitude, the band-to-band miss-registration error was not negligible; therefore, in the first step, they were registered. Then, to generate seamless orthomosaics, the registered images were aligned and radiometric normalization was implemented.

In order to produce a homogeneous orthomosaic, radiometric normalization as a part of the post-processing step is essential for generating uniformity in the block of images that acquired under a wide variety of environmental conditions. Therefore, in the radiometric calibration step, only the conversion of digital numbers to reflectance values is applied.

Radiometric calibration effects on plant classification and disease detection were evaluated in two scenarios. First, discrimination of the healthy and un-healthy classes was compared using T-test and entropy distances considering ground truth data collected from calibrated and un-calibrated orthomosaics. The experimental results showed that the effects of radiometric calibration on separability criteria using most spectral features were insignificant . In the other scenario, the radiometric calibration effects on the accuracy of classification were investigated. For this purpose, the best features were selected based on the separation criteria of the tree classes and the correlation between the features. The random forest classifier was applied to detect diseased trees. Experimental results showed insignificant differences in the classification results after radiometric calibration. At the Fasa study site, the overall accuracy and kappa values for un-calibrated and calibrated orthomosaic classifications were 96.49%, 0.941, 96.57% and 0.942, respectively. On the other study site, the overall accuracy and kappa values for un-calibrated and calibrated orthomosaic classifications were 95.58%, 0.913, 95.56% and 0.913.

As the results showed, radiometric calibration had a minor effect on the classification results. This can be attributed to the fact that images used for the classification were acquired at a single date with consistent atmospheric and sun illumination condition. Exclusion of radiometric calibration would substantially simplify UAV-based small-scale agricultural monitoring and disease detection processes. However, in case images from different dates or large areas are used for classification, radiometric calibration or image normalization might be required to improve classification accuracy.

Disclosure statement

No potential conflict of interest was reported by the authors.

ORCID

Farhad Samadzadegan http://orcid.org/0000-0003-3439-5648
Farzaneh Dadrass Javan http://orcid.org/0000-0002-0910-8160

References

Agüera, F., Carvajal, F., & Pérez, M. (2011). Measuring sunflower nitrogen status from an unmanned aerial vehicle-based system and an on the ground device. *International Archives of the Photogrammetry, Remote Sensing and Spatial Information Science*, *38*, 33–37.

Albetis, J., Duthoit, S., Guttler, F., Jacquin, A., Goulard, M., Poilvé, H., … Dedieu, G. (2017). Detection of Flavescence dorée grapevine disease using Unmanned Aerial Vehicle (UAV) multispectral imagery. *Remote Sensing*, *9*(4), 308. doi:10.3390/rs9040308

Ashourloo, D., Mobasheri, M.R., & Huete, A. (2014). Developing two spectral disease indices for detection of wheat leaf rust (Pucciniatriticina). *Remote Sensing*, *6*(6), 4723–4740. doi:10.3390/rs6064723

Baranowski, P., Jedryczka, M., Mazurek, W., Babula-Skowronska, D., Siedliska, A., & Kaczmarek, J. (2015). Hyperspectral and thermal imaging of oilseed rape (Brassica napus) response to fungal species of the genus Alternaria. *PloS One*, *10*(3), e0122913. doi:10.1371/journal.pone.0122913

Baret, F. (2016). Estimation of biophysical variables from satellite observations. In *Land surface remote sensing in agriculture and forest* (pp. 37–80). Elsevier.

Berni, J.A., Zarco-Tejada, P.J., Suárez, L., & Fereres, E. (2009). Thermal and narrowband multispectral remote sensing for vegetation monitoring from an unmanned aerial vehicle. *IEEE Transactions on Geoscience and Remote Sensing*, *47*(3), 722–738. doi:10.1109/TGRS.2008.2010457

Breiman, L. (2001). Random forests. *Machine Learning*, *45*(1), 5–32. doi:10.1023/A:1010933404324

Candiago, S., Remondino, F., De Giglio, M., Dubbini, M., & Gattelli, M. (2015). Evaluating multispectral images

and vegetation indices for precision farming applications from UAV images. *Remote Sensing*, *7*(4), 4026–4047. doi:10.3390/rs70404026

Cevallos-Cevallos, J.M., Futch, D.B., Shilts, T., Folimonova, S.Y., & Reyes-De-Corcuera, J.I. (2012). GC–MS metabolomic differentiation of selected citrus varieties with different sensitivity to citrus huanglongbing. *Plant Physiology and Biochemistry*, *53*, 69–76. doi:10.1016/j.plaphy.2012.01.010

Clemens, S.R. (2012). *Procedures for correcting digital camera imagery acquired by the AggieAir remote sensing platform*.

De Castro, A., Ehsani, R., Ploetz, R., Crane, J., & Abdulridha, J. (2015). Optimum spectral and geometric parameters for early detection of laurel wilt disease in avocado. *Remote Sensing of Environment*, *171*, 33–44. doi:10.1016/j.rse.2015.09.011

Feng, Q., Liu, J., & Gong, J. (2015). UAV remote sensing for urban vegetation mapping using random forest and texture analysis. *Remote Sensing*, *7*(1), 1074–1094. doi:10.3390/rs70101074

Franke, J., & Menz, G. (2007). Multi-temporal wheat disease detection by multi-spectral remote sensing. *Precision Agriculture*, *8*(3), 161–172. doi:10.1007/s11119-007-9036-y

Garcia-Ruiz, F., Sankaran, S., Maja, J.M., Lee, W.S., Rasmussen, J., & Ehsani, R. (2013). Comparison of two aerial imaging platforms for identification of Huanglongbing-infected citrus trees. *Computers and Electronics in Agriculture*, *91*, 106–115. doi:10.1016/j.compag.2012.12.002

Gehrke, S., & Beshah, B. (2016). Radiometric normalization of large airborne image data sets acquired by different sensor types. *International Archives of the Photogrammetry, Remote Sensing & Spatial Information Sciences*, *41*, *317–326*.

Glaser, J., Casas, J., Copenhaver, K., & Mueller, S. (2009). *Development of a broad landscape monitoring system using hyperspectral imagery to detect pest infestation*. Paper presented at the Hyperspectral Image and Signal Processing: Evolution in Remote Sensing, 2009. WHISPERS'09. First Workshop on, Grenoble, France.

Guyon, I., & Elisseeff, A. (2003). An introduction to variable and feature selection. *Journal of Machine Learning Research*, *3*(Mar), 1157–1182.

Haboudane, D., Miller, J.R., Pattey, E., Zarco-Tejada, P. J., & Strachan, I.B. (2004). Hyperspectral vegetation indices and novel algorithms for predicting green LAI of crop canopies: Modeling and validation in the context of precision agriculture. *Remote Sensing of Environment*, *90*(3), 337–352. doi:10.1016/j.rse.2003.12.013

Hart, W., & Myers, V. (1968). Infrared aerial color photography for detection of populations of brown soft scale in citrus groves 1 2 3. *Journal of Economic Entomology*, *61*(3), 617–624. doi:10.1093/jee/61.3.617

Hede, A.N.H., Kashiwaya, K., Koike, K., & Sakurai, S. (2015). A new vegetation index for detecting vegetation anomalies due to mineral deposits with application to a tropical forest area. *Remote Sensing of Environment*, *171*, 83–97. doi:10.1016/j.rse.2015.10.006

Honkavaara, E., Saari, H., Kaivosoja, J., Pölönen, I., Hakala, T., Litkey, P., … Pesonen, L. (2013). Processing and assessment of spectrometric, stereoscopic imagery collected using a lightweight UAV spectral camera for precision agriculture. *Remote Sensing*, *5*(10), 5006–5039. doi:10.3390/rs5105006

Huang, Y., Lan, Y., & Hoffmann, W. (2008). Use of airborne multi-spectral imagery in pest management systems. *Agricultural Engineering International: CIGR Journal, 10*, 1–14.

Jhan, J.-P., Rau, J.-Y., & Huang, C.-Y. (2016). Band-to-band registration and ortho-rectification of multilens/multispectral imagery: A case study of MiniMCA-12 acquired by a fixed-wing UAS. *ISPRS Journal of Photogrammetry and Remote Sensing*, *114*, 66–77. doi:10.1016/j.isprsjprs.2016.01.008

Jia, L., Yu, Z., Li, F., Gnyp, M., Koppe, W., Bareth, G., … Zhang, F. (2011). *Nitrogen status estimation of winter wheat by using an IKONOS satellite image in the north china plain*. Paper presented at the International Conference on Computer and Computing Technologies in Agriculture, Berlin, Heidelberg.

Joshi, A., Monnier, C., Betke, M., & Sclaroff, S. (2015). *A random forest approach to segmenting and classifying gestures*. Paper presented at the Automatic Face and Gesture Recognition (FG), 2015 11th IEEE International Conference and Workshops on, Ljubljana, Slovenia.

Joshi, P.C. (2011). Performance evaluation of vegetation indices using remotely sensed data. *International Journal of Geomatics and Geosciences*, *2*(1), 231.

Katti, A.R., Lee, W.S., Ehsani, R., & Yang, C. (2015). Band selection using forward feature selection algorithm for citrus Huanglongbing disease detection. *Journal of Biosystems Engineering*, *40*(4), 417–427. doi:10.5307/JBE.2015.40.4.417

Kelcey, J., & Lucieer, A. (2012). *Sensor correction and radiometric calibration of a 6-band multispectral imaging sensor for UAV remote sensing*. Paper presented at the The 12th Congress of the International Society for Photogrammetry and Remote Sensing, Melbourne, Australia.

Li, H., Lee, W.S., Wang, K., Ehsani, R., & Yang, C. (2014). 'Extended spectral angle mapping (ESAM)'for citrus greening disease detection using airborne hyperspectral imaging. *Precision Agriculture*, *15*(2), 162–183. doi:10.1007/s11119-013-9325-6

Lindeberg, T. (2012). *Scale invariant feature transform*.

Lu, S., Lu, X., Zhao, W., Liu, Y., Wang, Z., & Omasa, K. (2015). Comparing vegetation indices for remote chlorophyll measurement of white poplar and Chinese elm leaves with different adaxial and abaxial surfaces. *Journal of Experimental Botany*, *66*(18), 5625–5637. doi:10.1093/jxb/erv270

Mishra, A., Karimi, D., Ehsani, R., & Albrigo, L.G. (2011). Evaluation of an active optical sensor for detection of Huanglongbing (HLB) disease. *Biosystems Engineering*, *110*(3), 302–309. doi:10.1016/j.biosystemseng.2011.09.003

Miura, T., & Huete, A.R. (2009). Performance of three reflectance calibration methods for airborne hyperspectral spectrometer data. *Sensors*, *9*(2), 794–813. doi:10.3390/s90200794

Moscatello, S., Proietti, S., Buonaurio, R., Famiani, F., Raggi, V., Walker, R.P., & Battistelli, A. (2017). Peach leaf curl disease shifts sugar metabolism in severely infected leaves from source to sink. *Plant Physiology and Biochemistry*, *112*, 9–18. doi:10.1016/j.plaphy.2016.12.001

Näsi, R., Honkavaara, E., Lyytikäinen-Saarenmaa, P., Blomqvist, M., Litkey, P., Hakala, T., … Holopainen,

M. (2015). Using UAV-based photogrammetry and hyperspectral imaging for mapping bark beetle damage at tree-level. *Remote Sensing*, *7*(11), 15467–15493. doi:10.3390/rs71115467

Nesbit, P.R. (2014). *Uninhabited aerial vehicles and structure from motion: A fresh approach to photogrammetry*. Long Beach: California State University.

Nevalainen, O., Honkavaara, E., Tuominen, S., Viljanen, N., Hakala, T., Yu, X., … Imai, N.N. (2017). Individual tree detection and classification with UAV-based photogrammetric point clouds and hyperspectral imaging. *Remote Sensing*, *9*(3), 185. doi:10.3390/rs9030185

Nissen, E., Johnson, K.L., Fitzgerald, F.S., Morgan, M., & White, J. (2014). *Rapid-response or repeat-mode topography from aerial structure from motion*. Paper presented at the AGU Fall Meeting Abstracts, Sanfrancisco.

Onisimo, M., Timothy, D., & Omer, G. (2017). Remote sensing of crop health for food security in Africa: Potentials and constraints. *Remote Sensing Applications: Society and Environment, 8,* 231–239.

Pecknold, P.C. (2015). Peach Leaf Curl.

Psirofonia, P., Samaritakis, V., Eliopoulos, P., & Potamitis, I. (2017). Use of unmanned aerial vehicles for agricultural applications with emphasis on crop protection: Three novel case-studies. *International Journal of Agricultural Science and Technology*. doi:10.12783/ijast.2017.0501.03

Ranjitha, G., Srinivasan, M., & Rajesh, A. (2014). Detection and estimation of damage caused by thrips Thrips tabaci (Lind) of cotton using hyperspectral radiometer. *Agrotechnology*, *3*(1), 1–5.

REZAEIAN, M., AMIRFATTAHI, R., & SADRI, S. (2014). Semantic segmentation of aerial images using fusion of color and texture features.

Rodriguez-Galiano, V.F., Ghimire, B., Rogan, J., Chica-Olmo, M., & Rigol-Sanchez, J.P. (2012). An assessment of the effectiveness of a random forest classifier for land-cover classification. *ISPRS Journal of Photogrammetry and Remote Sensing*, *67*, 93–104. doi:10.1016/j.isprsjprs.2011.11.002

Sankaran, S., Ehsani, R., Inch, S.A., & Ploetz, R.C. (2012). Evaluation of visible-near infrared reflectance spectra of avocado leaves as a non-destructive sensing tool for detection of laurel wilt. *Plant Disease*, *96*(11), 1683–1689. doi:10.1094/PDIS-01-12-0030-RE

Sankaran, S., Maja, J.M., Buchanon, S., & Ehsani, R. (2013). Huanglongbing (citrus greening) detection using visible, near infrared and thermal imaging techniques. *Sensors*, *13*(2), 2117–2130. doi:10.3390/s130202117

Sankaran, S., Mishra, A., Ehsani, R., & Davis, C. (2010). A review of advanced techniques for detecting plant diseases. *Computers and Electronics in Agriculture*, *72*(1), 1–13. doi:10.1016/j.compag.2010.02.007

Sankaran, S., Mishra, A., Maja, J.M., & Ehsani, R. (2011). Visible-near infrared spectroscopy for detection of Huanglongbing in citrus orchards. *Computers and Electronics in Agriculture*, *77*(2), 127–134. doi:10.1016/j.compag.2011.03.004

Sarkar, S.K., Das, J., Ehsani, R., & Kumar, V. (2016). *Towards autonomous phytopathology: Outcomes and challenges of citrus greening disease detection through close-range remote sensing*. Paper presented at the Robotics and Automation (ICRA), 2016 IEEE International Conference on, Stockholm, Sweden.

Shi, J., Wang, J., & Xu, Y. (2011). Object-based change detection using georeferenced UAV images. *International Archives of the Photogrammetry, Remote Sensing and Spatial Information Science*, *38*, 177–182.

Smith, G.M., & Milton, E.J. (1999). The use of the empirical line method to calibrate remotely sensed data to reflectance. *International Journal of Remote Sensing*, *20*(13), 2653–2662. doi:10.1080/014311699211994

Wijesingha, J. (2016). Geometric quality assessment of multi-rotor unmanned aerial vehicle borne remote sensing products for precision agriculture. *Student thesis series INES*.

Wójtowicz, M., Wójtowicz, A., & Piekarczyk, J. (2016). Application of remote sensing methods in agriculture. *Communications in Biometry and Crop Science*, *11*, 31–50.

Ye, X., Sakai, K., ASADA, S.I., & Sasao, A. (2007). Use of airborne multispectral imagery to discriminate and map weed infestations in a citrus orchard. *Weed Biology and Management*, *7*(1), 23–30. doi:10.1111/j.1445-6664.2006.00236.x